

MonoMPC: Monocular Vision Based Navigation with Learned Collision Model and Risk-Aware Model Predictive Control

Basant Sharma, Prajyot Jadhav, Pranjal Paul, K.Madhava Krishna, Arun Kumar Singh

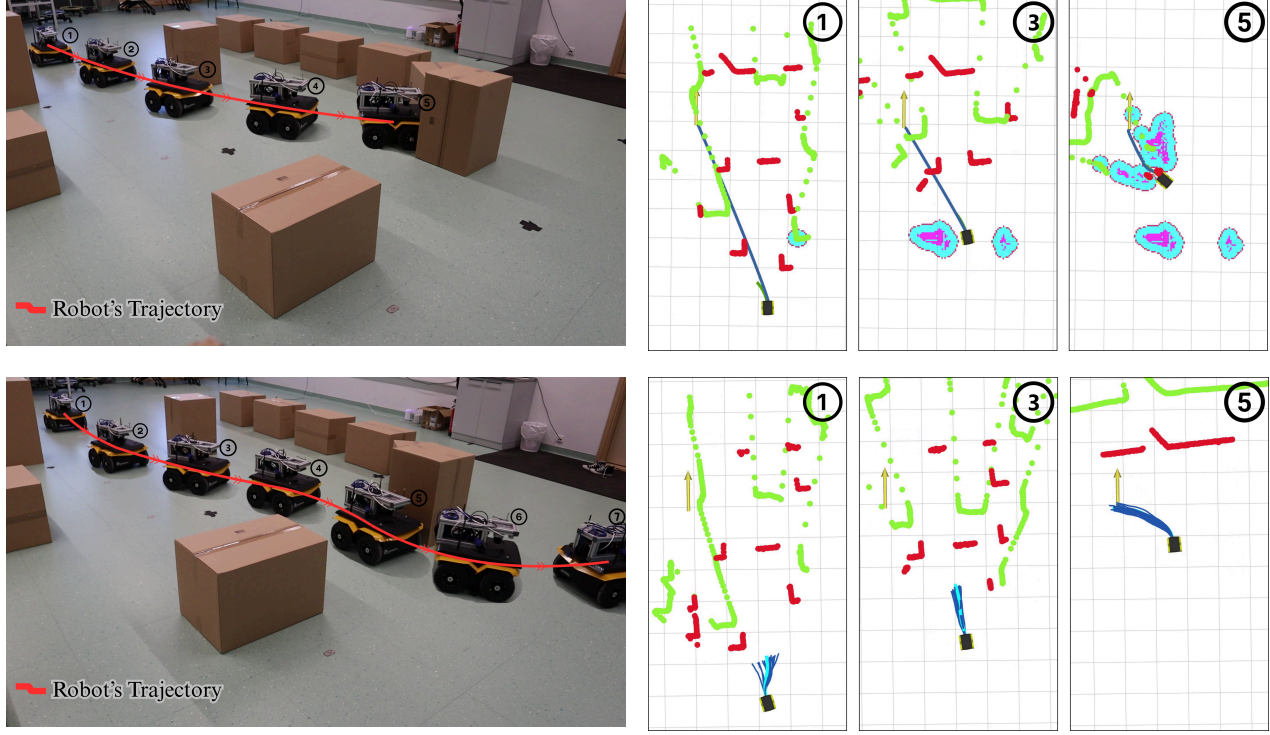


Fig. 1: Monocular navigation in cluttered environments using ROSNAV (top) vs. our approach (bottom). ROSNAV constructs cost maps directly from the estimated point cloud (green) generated by DepthAnything [1], which deviates significantly from the ground-truth (red), leading to incorrect free-space detection (e.g., top row, panel 3) and collisions. In contrast, our method treats the estimated point cloud as a conditioning input to a learned probabilistic collision model, integrated with a risk-aware MPC framework. Snapshots across time steps are shown for both methods (corresponding time indices are labeled).

Abstract— **Navigating unknown environments with a single RGB camera is challenging, as the lack of depth information prevents reliable collision-checking.** While some methods use estimated depth to build collision maps, we found that depth estimates from vision foundation models are too noisy for zero-shot navigation in cluttered environments.

We propose an alternative approach: instead of using noisy estimated depth for direct collision-checking, we use it as a rich context input to a learned collision model. This model predicts the distribution of minimum obstacle clearance that the robot can expect for a given control sequence. At inference, these predictions inform a risk-aware MPC planner that minimizes estimated collision risk. Our joint learning pipeline co-trains the collision model and risk metric using both safe and unsafe trajectories. Crucially, our joint-training ensures optimal variance in our collision model that improves navigation in highly cluttered environments. Consequently, real-world experiments show 9x and 7x improvements in success rates over NoMaD and the ROS stack, respectively. Ablation studies further validate

Pranjal, Madhava Krishna are with IIIT-Hyderabad. Basant, Prajyot, Arun are with the University of Tartu. This research was in part supported by grant PSG753 from Estonian Research Council, collaboration project LL-TAT21278 with Bolt Technologies and project TEM-TA101 funded by European Union and Estonian Research Council. Email:aks1812@gmail.com

the effectiveness of our design choices.

I. INTRODUCTION

Navigation in unknown environments using a monocular RGB camera is well-suited for lightweight robotic platforms like aerial or compact ground robots, where size, weight, and power constraints make LiDARs impractical. Vision-only setups reduce hardware complexity and energy usage, supporting longer missions and broader deployment in cost-sensitive settings. However, monocular navigation remains fundamentally challenging due to the absence of direct depth perception, which hampers reliable collision-checking essential for safe operation in cluttered environments.

Recent progress in vision foundation models like DepthAnything [1], [2] and ZoeDepth [3] has enabled depth prediction from a single RGB image, opening new avenues for monocular navigation. Prior work has used these depth estimates to build local 3D or collision maps for planning [4]. However, our experiments show that such depth predictions are often too noisy or inconsistent for reliable collision-checking, particularly in close-proximity scenarios where

small errors can result in collisions (see Fig. 1). In zero-shot settings—where the robot must generalize to unseen environments—these models fall short as standalone solutions.

In this work, we propose a novel approach to monocular navigation that reinterprets estimated depth not as a proxy for ground truth, but as an informative input to a learned probabilistic collision model. While monocular depth estimates may be noisy, they contain valuable structural cues. Our model takes the RGB image and a candidate control sequence as input and predicts a distribution over worst-case obstacle clearance along that trajectory. These predictions are used at inference time to estimate collision risk, which is minimized via a risk-aware model predictive control (MPC) planner to generate safe and goal-directed actions.

We propose a joint learning pipeline that co-trains the collision model and risk metric using both safe and unsafe trajectories. This ensures the model learns how its predictions impact downstream risk, providing valuable feedback that helps regularize variance to enable safe yet non-conservative behavior.

We validate our approach through real-world hardware experiments, showing substantial improvements in navigation success over strong baselines like NoMaD [5]—a diffusion-based end-to-end method—and the ROS navigation stack, which relies on estimated depth-based costmaps (Fig. 1). Ablation studies further highlight the impact of our design choices.

II. RELATED WORKS

In the following, we restrict our review to works that use only monocular camera for navigation and exclude those that rely on depth sensors or LiDARs.

A. End-to-End Approaches for Visual Navigation

A common approach in monocular visual navigation is to train end-to-end models that map RGB images directly to control outputs like velocity commands or waypoints. Many rely on supervised learning via behavioral cloning or imitation learning [6], [7], [8], [9], [10], [11]. While simple and appealing, these methods often generalize poorly, are sensitive to perception noise, and lack interpretability. They also omit explicit modeling of geometry, uncertainty, and constraints, making them data-hungry and hard to adapt. Recent methods like ViNT [12] and NoMaD [5] improve generalization by using image-conditioned diffusion models to generate trajectories from RGB input. However, they depend on high-quality supervision and do not model collision uncertainty.

Another class of approaches focuses on learning spatial representations from monocular input [4], [9], [10]. For example, [4] constructs a map from estimated depth and then performs planning over it. However, since our problem setting focuses on navigation in unknown environments without explicit map construction, such methods fall outside the scope of this work.

Deep reinforcement learning (DRL) has also been explored for visual navigation, particularly in unseen or partially known environments [13], [14], [15]. While DRL

enables flexible end-to-end learning from experience, it typically requires extensive training in simulation, careful reward shaping, and offers limited safety guarantees.

B. World Model-Based Approaches for Visual Navigation

World model-based methods [16], [17], [18] learn action-conditioned predictive models to simulate dynamics—predicting the next state given the current state and action—for downstream planning and control, rather than directly learning policies. [19] adopt a slightly different approach and propose a visual MPC controller that outputs a sequence of velocity commands based on the current image and a trajectory of subgoal images. Authors in [20] regress depth images and actions to collision probabilities which is then minimized within an MPC framework. Although theoretically, this approach can be extended to work with estimated depth, it is unclear how the associated noise will affect the efficiency of the overall pipeline. Moreover, we believe that predicting obstacle clearance distribution is easier than directly predicting collision probabilities, as the supervision data for the former can be easily obtained. Our design choice also allows us to use sophisticated statistical tools to capture collision risk from the clearance samples in an efficient manner.

C. Improvement Over State-of-the-Art:

Unlike end-to-end pipelines, our approach explicitly incorporates safety constraints by learning an action-conditioned collision model, placing us closer to world-model methods. However, unlike [16], [17], [18], [19], we model predictive uncertainty and collision risk, and introduce a novel method to learn task-aware uncertainty. Moreover, we also learn optimal parameters of our risk metric to improve the efficacy of our approach.

Most monocular navigation methods demonstrate results in simple environments like hallways. In contrast, we show—for the first time—robust and reliable navigation in cluttered settings typically requiring LiDAR or depth sensors.

III. MAIN ALGORITHMIC RESULTS

Symbols and Notations: We use small/upper case normal font to represent scalars. The bold-face small fonts represent vectors while upper-case variants represent matrices.

A. Vision-Based Navigation as Risk-Aware Trajectory Optimization

We frame monocular vision-based collision avoidance and goal reaching as the following trajectory optimization.

$$\min_{\mathbf{u}} w_1 c(\mathbf{x}) + w_2 r(d(\mathbf{u}, \mathbf{o})) + w_3 \|\mathbf{u}\|_2^2, \quad (1a)$$

$$\mathbf{x}_{k+1} = f(\mathbf{x}_k, \mathbf{u}_k), \quad (1b)$$

$$\mathbf{u}_{min} \leq \mathbf{u}_k \leq \mathbf{u}_{max} \forall k \quad (1c)$$

where $c(\cdot)$ represents the state-dependent cost function. The vector \mathbf{x}_k represents the state of the robot at time-step k . The vector \mathbf{x} is the concatenation of the states at different k . The function f represents the robot dynamics model. The control

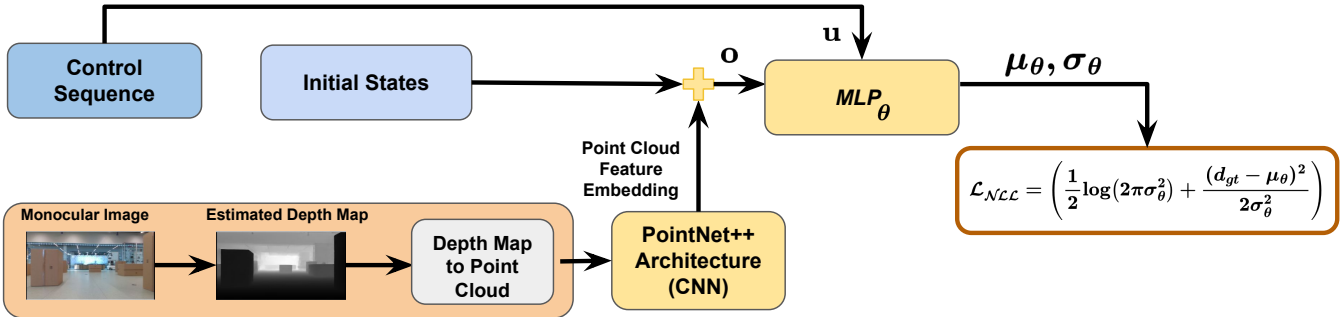


Fig. 3: Overview of baseline learning pipeline for our probabilistic collision model that predicts worst-case obstacle clearance along a trajectory. Given an RGB image and control sequence, we extract geometric features from the estimated point cloud using a pre-trained depth estimator and PointNet++. Combined with the initial robot state, these form the observation vector, which an MLP uses to predict the mean and variance of obstacle clearance. The learnable components (yellow blocks) are trained end-to-end using Gaussian negative log-likelihood loss.

inputs are represented by \mathbf{u}_k . The vector \mathbf{u} is formed by stacking \mathbf{u}_k at different time-step k respectively. The scalar function d represents a learned probabilistic collision model, which takes as input the observations \mathbf{o} and the control sequence \mathbf{u} and outputs a distribution of worst-case obstacle clearance along the trajectory resulting from \mathbf{u} . We discuss the details of the d in the subsequent sections. The first term in (1a) minimizes the state cost, typically addressing path-following errors. The second term captures collision-risk based on the predictions of d . The last term in (1a) penalizes large control inputs, and the weights w_i tune the robot's risk-seeking behavior. Control bounds are enforced through (1c). We construct a MPC feedback loop by solving (1a)-(1c) in a receding horizon manner from the current state.

B. Modeling Risk Through Chance-Constraints

We model the robot's footprint as a circular disk of radius d_o . Thus, we can define $h(d(\mathbf{u}, \mathbf{o})) = -d(\mathbf{u}, \mathbf{o}) + d_o \leq 0$ as the control and observation dependent collision-avoidance constraint. We define risk r in terms of so-called chance constraints. These have the general form of $P(h(d(\mathbf{u}, \mathbf{o})) \geq 0) \leq \varepsilon$, where P represents probability and ε is some constant. Thus, we define risk as:

$$r(h(d(\mathbf{u}, \mathbf{o}))) = P(h(d(\mathbf{u}, \mathbf{o}))) \geq 0 \quad (2)$$

Intuitively, our risk model captures the probability of collision constraints being violated for a given control sequence \mathbf{u} and current observation \mathbf{o} . Moreover, the risk depends on the distribution characterized by the collision model d . Our aim is to first learn a suitable d and then minimize the associated risk using (1a)-(1c).

A key challenge in using risk r as defined in (2) is that the left-hand side does not have an analytical form if the predictive distribution of $d(\mathbf{u}, \mathbf{o})$ departs significantly from Gaussian. Thus, in the next subsection, we present a surrogate risk model that is more tractable and can produce the same effect as r .

C. Maximum Mean Discrepancy(MMD) as parameterized risk metric

Let us define a constraint residual function as

$$\bar{h}(d(\mathbf{u}, \mathbf{o})) = \max(0, h(d(\mathbf{u}, \mathbf{o}))) \quad (3)$$

In the deterministic scenario, driving $\bar{h}(d(\mathbf{u}, \mathbf{o}))$ to zero will push $h(d(\mathbf{u}, \mathbf{o}))$ to the feasible boundary. In the stochastic case, (3) maps $d(\mathbf{u}, \mathbf{o})$ to a distribution of constraint residuals. Let $\bar{h}(d(\mathbf{u}, \mathbf{o})) \sim p_{\bar{h}}$. Although we don't know the parametric form for $p_{\bar{h}}$, we can be certain that its entire mass lies to the right of $\bar{h} = 0$. Moreover, as $P(h(d(\mathbf{u}, \mathbf{o})) \geq 0)$ approaches zero, $p_{\bar{h}}$ converges to a Dirac-Delta distribution p_{δ} [21]. In other words, one way of reducing risk is to minimize the difference between $p_{\bar{h}}$ and p_{δ} . We formulate this distribution matching through the lens of Maximum Mean Discrepancy (MMD) [22], [21] and use the following surrogate for the collision-risk proposed in [21], [23].

$$r \approx r_{MMD}^{emp} = \|\hat{\mu}[\bar{h}] - \hat{\mu}[\delta]\|_{\mathcal{H}}^2, \quad (4)$$

where, $\hat{\mu}[\bar{h}]$ is called the empirical RKHS embedding of $p_{\bar{h}}$. It is computed through the following expression

$$\hat{\mu}[\bar{h}] = \sum_{i=1}^{i=N} \frac{1}{N} K_{\lambda}(\cdot | \bar{h}, .), \quad (5)$$

where, $i\bar{h} = \bar{h}(i d(\mathbf{u}, \mathbf{o}))$ and $i d$ are the samples drawn from the predictive distribution characterized by d . In a similar manner, $\hat{\mu}[\delta]$ is computed based on the N samples of δ drawn from p_{δ} ¹. For any given N , as $r_{MMD}^{emp} \rightarrow 0$, $p_{\bar{h}} \rightarrow p_{\delta}$. Thus our aim is to compute a control sequence \mathbf{u} which leads to as low as possible r_{MMD}^{emp} .

The K_{λ} is a positive definite function in RKHS known as the kernel function with the "reproducing" property (6) [22], where $\langle \cdot \rangle$ represents the inner product. Throughout this paper, we have used Laplacian kernel for which λ represents the kernel width.

$$K_{\lambda}(\mathbf{z}, \mathbf{z}') = \langle K_{\lambda}(\mathbf{z}, \cdot), K_{\lambda}(\mathbf{z}', \cdot) \rangle_{\mathcal{H}} \quad (6)$$

Importance of Kernel Parameter: The kernel parameter λ critically controls the MMD metric, r_{MMD}^{emp} , by shaping the embeddings $\hat{\mu}[\bar{h}]$ and $\hat{\mu}[\delta]$. An overly large λ causes the embeddings to collapse to a constant, making them indistinguishable and insensitive to collision risk. Conversely, a λ that is too small makes the embeddings artificially

¹We can approximate p_{δ} through a Gaussian $\mathcal{N}(0, \epsilon)$, with an extremely small covariance $\epsilon \approx 10^{-5}$.

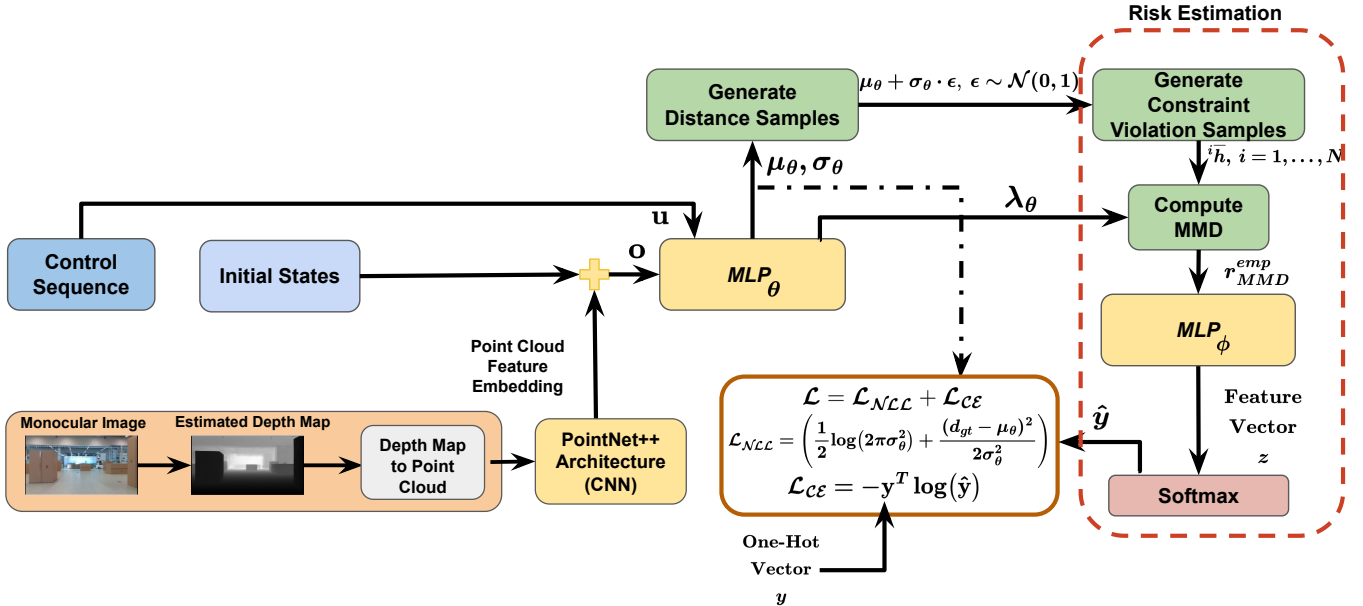


Fig. 4: Overview of our task-aware learning of probabilistic collision model. The previous baseline model of Fig.3 had a weak supervision on predicted variance due to the absence of ground-truth uncertainty, often resulting in over- or underconfident predictions. To address this, we introduce downstream supervision via collision risk estimation. The observation vector and control sequence are passed through MLP_θ to predict the mean, variance, and a kernel parameter. Using the reparameterization trick, we generate obstacle clearance samples to compute constraint violations, forming an MMD-based risk representation. This is processed by MLP_ϕ , followed by a softmax layer. The learnable parts shown in yellow are trained end-to-end with Gaussian NLL and a cross-entropy loss.

distinct, leading to overly conservative behavior that flags open spaces as high-risk. To resolve this, our approach learns to predict an optimal λ directly from current observations and control sequences (Section III-E, Fig.4).

D. Learning the Collision Model: The Baseline Approach

This section presents our approach for learning a probabilistic collision model $d(\mathbf{u}, \mathbf{o})$ which quantifies the worst-case obstacle clearance along a given trajectory. We model it as a Gaussian random variable with mean $\mu_\theta(\mathbf{u}, \mathbf{o})$ and variance $\sigma_\theta(\mathbf{u}, \mathbf{o})$, both of which are designed as feed-forward neural networks parameterized by weight θ . Our design choice allows us to capture the noise in the observation \mathbf{o} primarily stemming from the estimated point-cloud.

The detailed architecture is shown in Fig. 3. It consists of a pre-trained depth estimator that takes in RGB image and produces a depth-map. The depth-map is converted to a 2D point cloud and passed through PointNet++ [24] to get a feature embedding. We concatenate PointNet++ features with the initial state to get the full observation vector \mathbf{o} , which is then passed along with control sequence \mathbf{u} to a Multi-Layer Perceptron (MLP) to get $\mu_\theta(\mathbf{u}, \mathbf{o})$ and $\sigma_\theta(\mathbf{u}, \mathbf{o})$. Both PointNet++ and MLP are trained in end-to-end manner using the following negative log-likelihood (NLL) function.

$$\mathcal{L}_{NLL} = \left(\frac{1}{2} \log(2\pi\sigma_\theta^2) + \frac{(d_{gt} - \mu_\theta)^2}{2\sigma_\theta^2} \right), \quad (7)$$

where d_{gt} represents the ground-truth worst-case obstacle clearance along a given trajectory. We explain how these are obtained in Section IV.

E. Learning the Collision Model: The Down-Stream Task-Aware Approach

The core limitation of training with just the baseline NLL loss (7) is that the supervision on variance is rather weak since there is no ground truth variance available. Moreover, the training process is unaware of how its predictions are leveraged by the downstream task. Depending on how the training proceeds, the trained model can be either underconfident (high-variance) or overconfident (low-variance). For example, consider a scene where the actual d_{gt} signifies a collision-free scenario. That is $h(d_{gt}) = -d_{gt} + d_0 \leq 0$. Now, imagine that for this situation, the network of Fig.3 predicts a $\mu_\theta(\mathbf{u}, \mathbf{o})$ which is very close to d_{gt} but the variance is unreasonably higher. In such a case, the collision-free scenario will be incorrectly assigned high-risk due to uncertainty stemming from a higher variance.

The training process described in this section is designed to overcome the above described issues. Our main insight is that the supervision on variance can and should come from the downstream task of estimating collision risk based on the predicted σ_θ . To this end, we present the modified architecture in Fig. 4, which is obtained by adding a risk estimation head to the baseline architecture of Fig.3. During training time, we use the predicted $\mu_\theta(\mathbf{u}, \mathbf{o})$, $\sigma_\theta(\mathbf{u}, \mathbf{o})$ to generate samples d^i of the random variable $d(\mathbf{u}, \mathbf{o})$. We use the re-parameterization trick (8a) to generate samples in a differentiable manner. The samples d^i should characterize zero risk if the associated d_{gt} is indeed collision-free. On the other hand, the samples should lead to a high risk value if d_{gt} is insufficient for collision avoidance. We can interpret this

Algorithm 1: Sampling-Based Optimizer to Solve (1a)-(1c)

```

1  $M$  = Maximum number of iterations
2 Initiate mean  ${}^m\nu, {}^m\Sigma$ , at iteration  $m = 0$  for sampling control inputs  $\mathbf{u}$ ; Given observation vector  $\mathbf{o}$ , trained neural
   network  $\theta$ (Fig.4)
3 for  $m = 1, m \leq M, m++$  do
4   Initialize  $CostList = []$ 
5   Draw batch of  $n$  control sequences  $(\mathbf{u}_1, \mathbf{u}_2, \mathbf{u}_q, \dots, \mathbf{u}_n)$  from  $\mathcal{N}({}^m\nu, {}^m\Sigma)$ 
6   Query collision model  $\forall \mathbf{u}_q: (\mu_{\theta,q}, \sigma_{\theta,q}, \lambda_{\theta,q}) = \text{MLP}_{\theta}(\mathbf{u}_q, \mathbf{o})$  //  $\text{MLP}_{\theta}$  denotes the learned model
      whose output  $\mu_{\theta,q}, \sigma_{\theta,q}, \lambda_{\theta,q}$  denotes the predicted mean, predicted variance and
      the kernel parameter, respectively, for each control sequence  $\mathbf{u}_q$ 
7   Compute  $N$  distance samples  ${}^i d_q \sim \mathcal{N}(\mu_q, \sigma_q)$ ,  $\forall i = 1, \dots, N$  and subsequently  $N$  constraint violation samples
       ${}^i \bar{h}_q$ . Repeat this process  $\forall q = (1, 2, \dots, n)$  //  ${}^i d_q$  denotes  $i$ -th obstacle clearance sample
      corresponding to the  $q$ -th control sequence. Similarly for  ${}^i \bar{h}_q$ 
8   Compute  $\hat{\mu}_q[{}^i \bar{h}_q]$  over the constraint violation samples  ${}^i \bar{h}_q$  through (5) and subsequently  $r_{MMD,q}^{emp}$ . Repeat this
       $\forall q = (1, 2, \dots, n)$  // Compute the MMD-based surrogate for collision risk for each  $q$ 
9   Generate state trajectories  $\mathbf{x}_q(\mathbf{u}_q)$ ,  $\forall q = (1, 2, \dots, n)$ 
10   $ConstraintEliteSet \leftarrow$  Select top  $n_c$  batch of  $\mathbf{u}_q, \mathbf{x}_q$  with lowest  $r_{MMD,q}^{emp}$  // We sort control
      sequences  $\mathbf{u}_q$  and trajectories  $\mathbf{x}_q$  by lowest  $r_{MMD,q}^{emp}$  values.
11  Define  $c_q = w_1 c(\mathbf{x}_q) + w_2 r_{MMD,q}^{emp} + w_3 \|\mathbf{u}_q\|_2^2$ 
12   $cost \leftarrow c_q$ ,  $\forall q$  in the  $ConstraintEliteSet$ 
13  append each computed  $cost$  to  $CostList$ 
14   $EliteSet \leftarrow$  Select top  $n_e$  samples of  $(\mathbf{u}_q, \mathbf{x}_q)$  with lowest cost from  $CostList$ .
15   $({}^{m+1}\nu, {}^{m+1}\Sigma) \leftarrow$  Update distribution based on  $EliteSet$ 
16 end
17 return Control inputs  $\mathbf{u}_q$  and  $\mathbf{x}_q$  corresponding to lowest cost in the  $EliteSet$ 

```

requirement as a two class classification problem conditioned on the samples ${}^i d$ and implicitly on the predicted variance $\sigma_{\theta}(\mathbf{u}, \mathbf{o})$. The risk estimation head of Fig.4 performs exactly this role.

The risk estimation head estimates collision constraint violations from ${}^i d$ ((8b)-(8c)). Using these violations and the predicted kernel width λ_{θ} , the empirical MMD risk r_{MMD}^{emp} is computed. This risk is then passed through an MLP to yield a 2D feature vector \mathbf{z} , which a softmax layer normalizes to $\hat{\mathbf{y}}$. The ground-truth label for $\hat{\mathbf{y}}$ is given by \mathbf{y} and is computed through (9)

$${}^i d = \mu_{\theta} + \sigma_{\theta} \cdot {}^i \epsilon, \quad {}^i \epsilon \sim \mathcal{N}(0, 1), \quad \forall i = 1, \dots, N \quad (8a)$$

$${}^i h({}^i d) = -{}^i d + d_o \quad (8b)$$

$${}^i \bar{h}({}^i d) = \max(0, {}^i h({}^i d)) \quad (8c)$$

$$\mathbf{y} = \begin{cases} [0, 1]^T, & \text{if } -d_{gt} + d_o \leq 0 \\ [1, 0]^T, & \text{if } -d_{gt} + d_o > 0 \end{cases} \quad (9)$$

The architecture of Fig.4 is trained with a combination of NLL and a cross-entropy loss (10). The latter acts as an implicit task-aware regularization on the predicted $\sigma_{\theta}(\mathbf{u}, \mathbf{o})$.

$$\mathcal{L} = \mathcal{L}_{NLL} + \mathcal{L}_{CE}, \quad \mathcal{L}_{CE} = -\mathbf{y}^T \log(\hat{\mathbf{y}}) \quad (10)$$

F. Overall Approach

Alg.1 presents our overall approach wherein we solve (1a)-(1c) using the trained neural worst-case obstacle clearance model as our collision predictor. We adopt a sampling-based optimizer based on [25], wherein a batch of control sequences are drawn from a distribution which is gradually refined across iterations.

The algorithm initializes the sampling distribution (Line 2) and samples control inputs (Line 5), which are passed through a trained neural network (Line 6) to predict the mean $\mu_{\theta,q}$ and variance $\sigma_{\theta,q}$ associated with the distribution of obstacle clearances, as well as the kernel hyperparameter $\lambda_{\theta,q}$. These predictions generate N distance samples ${}^i d_q$, constraint violations ${}^i \bar{h}_q$ (Line 7), and subsequently $r_{MMD,q}^{emp}$ (Line 8). State trajectories $\mathbf{x}_q(\mathbf{u}_q)$ are then generated using the robot dynamics (Line 9). The n_c lowest-risk samples form the $ConstraintEliteSet$ (Line 10), from which costs are evaluated and stored (Lines 11–13). Finally, the top n_e samples form the $EliteSet$ (Line 14) used to update the sampling distribution (Line 15) following [25].

IV. VALIDATION AND BENCHMARKING

A. Implementation Details

We implemented Alg.1 in Python using Jax [26] as the GPU-accelerated linear algebra back-end. The state cost consists

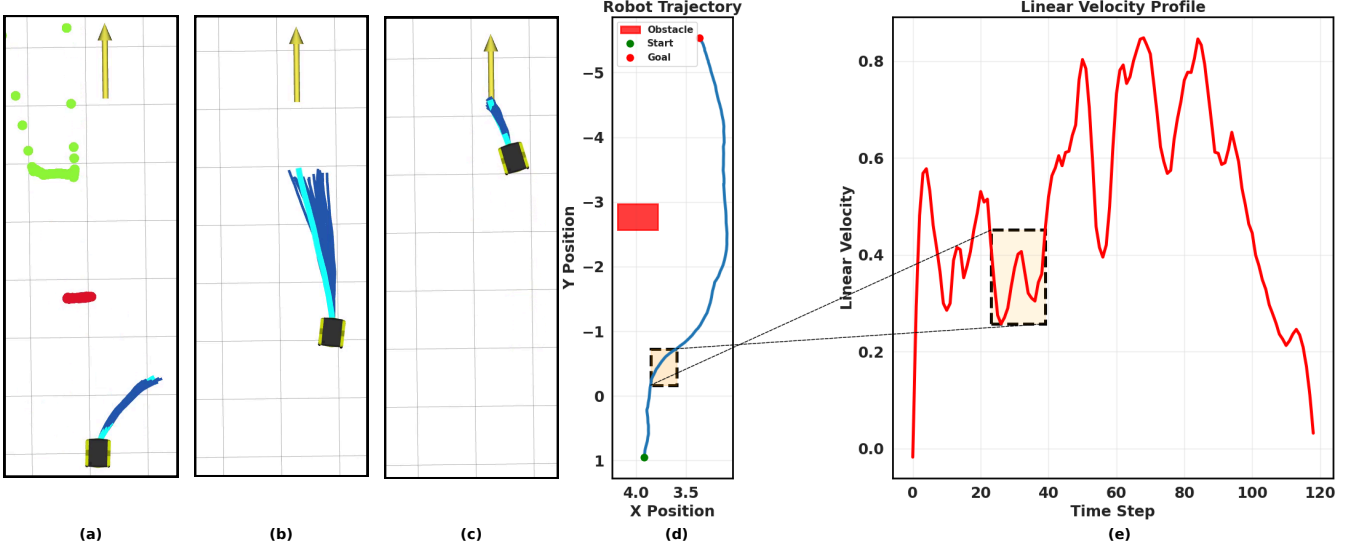


Fig. 5: We evaluate our learned collision model's and risk-aware MPC performance in a simple scenario. In (a), although the estimated point cloud (green) appears farther than the ground truth (red), the robot slows down (e) and steers away from the obstacle (a-d), successfully avoiding collision. This demonstrates our learned collision model's ability to output a well-regularized distribution over worst-case obstacle clearance. Note that in (b) and (c) the obstacle is outside the field-of-view of the robot and hence the resulting point clouds are absent.

of a running goal cost and has the following form:

$$c(\mathbf{x}) = \sum_k (x_k - x_f)^2 + (y_k - y_f)^2 \quad (11)$$

where x_f, y_f denote the end-point coordinates. We used Alg.1 in a receding horizon manner from the current state to create a MPC feedback loop.

1) Data Collection Pipeline:

a) Data Collection: We collected two datasets: one via teleoperation and another using a custom planner. Data were recorded at 10 Hz, with each sample consisting of :

- A standardized estimated point cloud of shape 300×2 ,
- Robot state $\mathbf{x} = (x, y, \psi, v, \omega)$, where (x, y) is position, ψ is heading, and v, ω are the linear and angular velocities (sampled uniformly from $\mathcal{U}[-1, 1]$ and clipped to $[0, 1]$ m/s and $[-1, 1]$ rad/s, respectively),
- A control sequence $\mathbf{u} = (\mathbf{v}, \omega)$ (see IV-A.1.b),
- Ground-truth clearance d_{gt} from LiDAR (see IV-A.1.c).

b) Control Sequence Generation: Each sample includes $N_p = 50$ control sequences over a 5s horizon at $\Delta t = 0.1$ s. Control sequences $\mathbf{u} = (\mathbf{v}, \omega)$ are generated as $\mathbf{u} \sim \mathcal{U}([-1.0, 1.0])$ with \mathbf{v} clipped to $[0, 1]$ m/s. To get the resulting trajectories the robot state evolves via:

$$\begin{bmatrix} x_{k+1} \\ y_{k+1} \\ \psi_{k+1} \end{bmatrix} = \begin{bmatrix} x_k + v_k \cos(\psi_k) \Delta t \\ y_k + v_k \sin(\psi_k) \Delta t \\ \psi_k + \omega_k \Delta t \end{bmatrix} \quad (12)$$

c) Ground-Truth Distance Computation: For each trajectory resulting from the j -th control sequence $\mathbf{u}_j = (\mathbf{v}_j, \omega_j)$, $\forall j = 1, \dots, N_p$, the minimum distance to the LiDAR point cloud $\mathcal{P}_{\text{LiDAR}}$ is:

$$d_{gt,j} = \min_{k, \mathbf{p} \in \mathcal{P}_{\text{LiDAR}}} \left\| \begin{bmatrix} x_{k,j} \\ y_{k,j} \end{bmatrix} - \mathbf{p} \right\|_2 \quad (13)$$

2) Benchmarking Environment: We evaluate our approach in a model predictive control (MPC) framework using a Clearpath Jackal robot equipped with an Intel RealSense D435i RGB-D camera (RGB-only input, 69° horizontal FOV). For visualization and analysis, LiDAR data was recorded from a SICK TIM551 2D sensor. The system ran on ROS Noetic with an NVIDIA RTX 3080 GPU laptop connected to the Jackal over a local network. Depth estimation was performed in real time using TensorRT-accelerated Depth-Anything-V2 [1]. Experiments were conducted in indoor environments with static cardboard boxes to simulate clutter.

B. Validation on a simple example

Fig.5 shows a simple scenario where the robot needs to avoid just a single static obstacle. As can be seen, the estimated point-cloud (green) is at a large offset from the ground-truth (red) provided by the LiDAR. In spite of this, our learned collision model correctly predicts the worst-case obstacle clearance for different control samples and successfully guides the robot away from the obstacle (Fig.5(a)-(d)). Moreover, Fig.5(c)-(d) shows that our MPC framework is able to slow down the robot near the obstacles to minimize risk but compensates goal-reaching by generating higher speeds in free-space.

C. Comparison with ROS Navigation Stack (ROSNAV)

In this subsection, we compare our method with classical planning stacks that use estimated point clouds to build costmaps. Specifically, we use navfn² as the global planner and Dynamic Window Approach (DWA) [27] as the local planner from ROSNAV. To ensure fairness with our planner (Alg.1), which constrains linear velocities to $[0, 1]$ m/s, we

²<https://wiki.ros.org/navfn>

TABLE I: Comparison with ROS Navigation Stack
(60 experiments)

Method	% Collisions	% Stuck	Avg. Speed (m/s)	Max. Speed (m/s)
Alg.1 with r_{MMD}^{emp} -based Augmented Model	6.6	0	0.32	1.02
ROSNAV (0.5 m/s)	25	51.6	0.38	0.59
ROSNAV (1 m/s)	48.3	48.3	0.73	1.15

evaluate ROSNAV under two speed limits: 0.5 m/s and 1.0 m/s.

We observed two main failure modes with ROSNAV, both arising from inaccuracies in the estimated depth. First, due to a significant and stochastic offset between the estimated and ground-truth point clouds, dependent on obstacle placement and camera field-of-view, the robot often misidentifies free space (Fig. 1(a)(3-4)), resulting in collisions or getting stuck. Second, as shown in our accompanying video, the goal sometimes lies within inflated costmaps derived from noisy estimates, preventing any feasible path from being generated. These issues stem from the non-trivial, time-varying nature of the estimation error, which cannot be resolved with simple heuristics.

Table I quantifies these issues: ROSNAV suffers frequent collisions, particularly at higher speeds, and fails to generate feasible plans in a substantial number of trials. In contrast, our MMD-based planner achieves up to 7x fewer collisions and consistently avoids getting stuck.

D. Comparison with End-to-End Model NoMaD [5]

NoMaD [5] is a foundational model for image-based goal-directed navigation. To focus on its obstacle avoidance capabilities, we evaluate it in simplified scenarios where the goal lies directly ahead and is visible from the start position, requiring only obstacle avoidance. For fair comparison, we finetune NoMaD on data from environments similar to those in Fig. 1.

Fig.6 shows a qualitative comparison. While NoMaD trajectories tend to steer away from obstacles, they often lack the precision needed for safe navigation. In contrast, our method explicitly accounts for collision risk, resulting in safer behavior. TableII shows that NoMaD completes very few runs without collision, consistent with prior results [4], which report over 50% collision rates even in simpler hallway environments. Our settings were more complex, leading to even higher failure rates.

E. Ablations

Table III shows that our task-aware model (Fig.4) achieves nearly 4x fewer collisions than the baseline (Fig.3) in the same test environment (Fig.1). This improvement stems from better variance regularization—both models predict similar means, but our model’s lower variance enables safer, less conservative plans (Fig.7). The baseline’s higher variance often causes free space to be misclassified as high-risk, making MPC planning infeasible. Simply penalizing variance

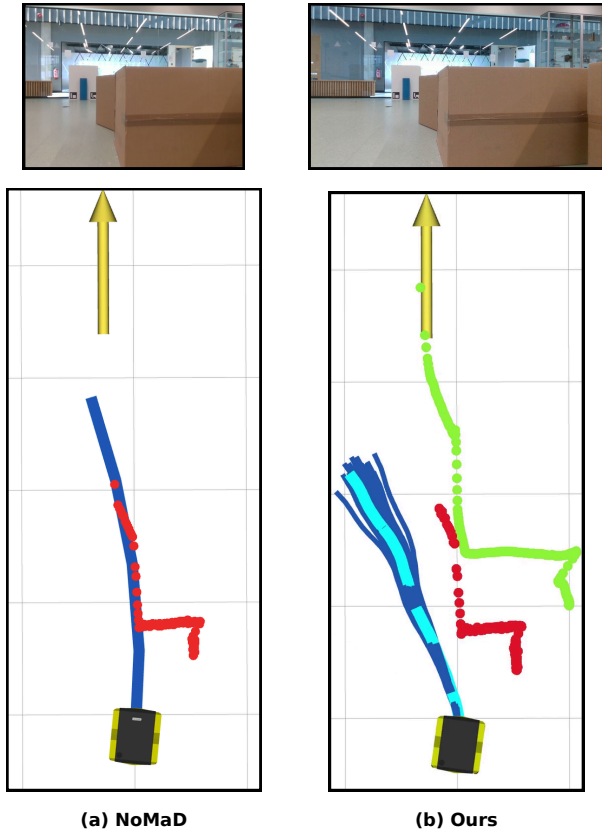


Fig. 6: The top row shows the camera-feed when running NoMaD and our pipeline. The figure illustrates that the trajectory generated by NoMaD in (a) attempts to avoid the obstacle (red point cloud) but fails to execute a precise collision avoidance maneuver. In contrast, our method in (b) successfully deviates from the obstacle, despite the estimated point cloud (green) being offset from the ground truth. This is attributed to our learned collision model’s ability to account for uncertainty in the estimated point cloud and accurately predict the worst-case obstacle clearance.

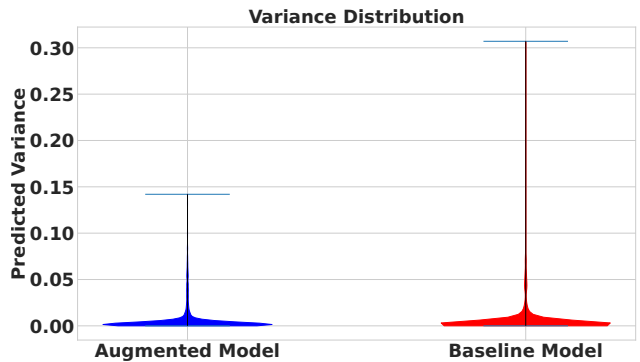


Fig. 7: The figure shows violin plots comparing the predicted variance distributions of the baseline and augmented models. The baseline model, trained only with an NLL loss, exhibits a broader spread—indicating overestimation and poor regularization of variance. In contrast, the augmented model yields a tighter distribution, reflecting task-aware variance regularization achieved through downstream risk supervision.

in the loss (7) leads to variance collapse and overconfidence; with near-zero variance, the model becomes effectively deterministic and fails to capture risk (Table III, row 3). In contrast, our task-aware approach learns a variance that is well aligned with safe navigation.

TABLE II: Comparison with NoMaD (60 experiments)

Method	% Collisions	% Stuck	Avg. Speed (m/s)	Max. Speed (m/s)
Alg.1 with \mathcal{F}_{MMD}^{emp} -based Augmented Model	8.3	0	0.28	1.05
NoMaD [5]	81.6	0	0.46	0.58

TABLE III: Ablations (60 experiments)

Method	% Collisions	% Stuck	Avg. Speed (m/s)	Max. Speed (m/s)
Alg.1 with \mathcal{F}_{MMD}^{emp} -based Augmented Model (Fig.4)	6.6	0	0.32	1.02
Alg.1 with Baseline Model(Fig.3)	28.3	0	0.35	0.94
DET	41.5	0	0.52	1.01

V. CONCLUSIONS AND FUTURE WORK

Monocular RGB-based navigation is challenging due to unreliable depth, which hinders safe collision-checking. While vision-based depth offers structural cues, its noise limits direct use. We propose a risk-aware framework that uses estimated depth as input to a probabilistic collision model, predicting worst-case obstacle clearance distributions. To regularize uncertainty, we jointly train the model and risk metric on safe and unsafe trajectories. At test time, an MPC planner uses these predictions to generate safe, goal-directed actions. Real-world experiments show our approach outperforms strong baselines like NoMaD and the ROS Navigation Stack using only monocular RGB input.

While demonstrated on a 2D ground robot, our approach readily extends to higher-dimensional platforms like quadrotors. Future directions include handling dynamic environments with time-varying collision models, accelerating planning via imitation learning, and exploring alternatives for capturing epistemic uncertainty beyond computationally costly model ensembling. We also plan to evaluate our collision model with other risk-aware MPC frameworks, such as those based on minimizing Conditional Value at Risk or enforcing chance-constraints.

REFERENCES

- [1] L. Yang, B. Kang, Z. Huang, Z. Zhao, X. Xu, J. Feng, and H. Zhao, “Depth anything v2,” in *Advances in Neural Information Processing Systems*, A. Globerson, L. Mackey, D. Belgrave, A. Fan, U. Paquet, J. Tomczak, and C. Zhang, Eds., vol. 37. Curran Associates, Inc., 2024, pp. 21 875–21 911. [Online]. Available: https://proceedings.neurips.cc/paper_files/paper/2024/file/26cfcd8fe6fd75cc53e92963a656c58-Paper-Conference.pdf
- [2] L. Yang, B. Kang, Z. Huang, X. Xu, J. Feng, and H. Zhao, “Depth anything: Unleashing the power of large-scale unlabeled data,” in *CVPR*, 2024.
- [3] S. F. Bhat, R. Birlk, D. Wofk, P. Wonka, and M. Müller, “Zoedepth: Zero-shot transfer by combining relative and metric depth,” 2023. [Online]. Available: <https://arxiv.org/abs/2302.12288>
- [4] N. Simon and A. Majumdar, “Mononav: Mav navigation via monocular depth estimation and reconstruction,” in *Symposium on Experimental Robotics (ISER)*, 2023. [Online]. Available: <https://arxiv.org/abs/2311.14100>
- [5] A. Sridhar, D. Shah, C. Glossop, and S. Levine, “Nomad: Goal masked diffusion policies for navigation and exploration,” in *2024 IEEE International Conference on Robotics and Automation (ICRA)*, 2024, pp. 63–70.
- [6] F. Codevilla, M. Müller, A. López, V. Koltun, and A. Dosovitskiy, “End-to-end driving via conditional imitation learning,” in *2018 IEEE International Conference on Robotics and Automation (ICRA)*, 2018, pp. 4693–4700.
- [7] A. Loquercio, A. I. Maqueda, C. R. del Blanco, and D. Scaramuzza, “Dronet: Learning to fly by driving,” *IEEE Robotics and Automation Letters*, vol. 3, no. 2, pp. 1088–1095, 2018.
- [8] D. Chen, B. Zhou, V. Koltun, and P. Krähenbühl, “Learning by cheating,” in *Conference on Robot Learning*. PMLR, 2020, pp. 66–75.
- [9] D. S. Chaplot, D. Gandhi, S. Gupta, A. Gupta, and R. Salakhutdinov, “Learning to explore using active neural slam,” in *International Conference on Learning Representations (ICLR)*, 2020.
- [10] D. S. Chaplot, R. Salakhutdinov, A. Gupta, and S. Gupta, “Neural topological slam for visual navigation,” in *CVPR*, 2020.
- [11] F. Sadeghi and S. Levine, “Cad2rl: Real single-image flight without a single real image,” in *Proceedings of Robotics: Science and Systems*, Cambridge, Massachusetts, July 2017.
- [12] D. Shah, A. Sridhar, N. Dashora, K. Stachowicz, K. Black, N. Hirose, and S. Levine, “ViNT: A foundation model for visual navigation,” in *7th Annual Conference on Robot Learning*, 2023. [Online]. Available: <https://arxiv.org/abs/2306.14846>
- [13] Y. Zhu, R. Mottaghi, E. Kolve, J. J. Lim, A. Gupta, L. Fei-Fei, and A. Farhadi, “Target-driven visual navigation in indoor scenes using deep reinforcement learning,” in *2017 IEEE International Conference on Robotics and Automation (ICRA)*, 2017, pp. 3357–3364.
- [14] G. Kahn, A. Villaflor, B. Ding, P. Abbeel, and S. Levine, “Self-supervised deep reinforcement learning with generalized computation graphs for robot navigation,” in *2018 IEEE International Conference on Robotics and Automation (ICRA)*, 2018, pp. 5129–5136.
- [15] S. Lian and F. Zhang, “Tdanet: Target-directed attention network for object-goal visual navigation with zero-shot ability,” *IEEE Robotics and Automation Letters*, vol. 9, no. 9, pp. 8075–8082, 2024.
- [16] A. Bar, G. Zhou, D. Tran, T. Darrell, and Y. LeCun, “Navigation world models,” in *Proceedings of the Computer Vision and Pattern Recognition Conference (CVPR)*, June 2025, pp. 15 791–15 801.
- [17] N. Hansen, H. Su, and X. Wang, “Td-mpc2: Scalable, robust world models for continuous control,” in *International Conference on Learning Representations (ICLR)*, 2024.
- [18] P. Wu, A. Escontrela, D. Hafner, K. Goldberg, and P. Abbeel, “Day-dreamer: World models for physical robot learning,” *Conference on Robot Learning*, 2022.
- [19] N. Hirose, F. Xia, R. Martín-Martín, A. Sadeghian, and S. Savarese, “Deep visual mpc-policy learning for navigation,” *IEEE Robotics and Automation Letters*, vol. 4, no. 4, pp. 3184–3191, 2019.
- [20] M. Jacquet and K. Alexis, “N-mpc for deep neural network-based collision avoidance exploiting depth images,” in *2024 IEEE International Conference on Robotics and Automation (ICRA)*. IEEE, 2024, pp. 13 536–13 542.
- [21] B. Sharma and A. K. Singh, “Trajectory optimization under stochastic dynamics leveraging maximum mean discrepancy,” *IEEE Robotics and Automation Letters*, vol. 10, no. 6, pp. 6079–6086, 2025.
- [22] A. Gretton, K. M. Borgwardt, M. J. Rasch, B. Schölkopf, and A. Smola, “A kernel two-sample test,” *J. Mach. Learn. Res.*, vol. 13, no. null, p. 723–773, 2012.
- [23] B. Sharma and A. K. Singh, “Mmd-opt : Maximum mean discrepancy based sample efficient collision risk minimization for autonomous driving,” *IEEE Transactions on Automation Science and Engineering*, pp. 1–1, 2025.
- [24] C. R. Qi, L. Yi, H. Su, and L. J. Guibas, “Pointnet++: Deep hierarchical feature learning on point sets in a metric space,” in *Advances in Neural Information Processing Systems*, I. Guyon, U. V. Luxburg, S. Bengio, H. Wallach, R. Fergus, S. Vishwanathan, and R. Garnett, Eds., vol. 30. Curran Associates, Inc., 2017. [Online]. Available: https://proceedings.neurips.cc/paper_files/paper/2017/file/d8bf84be3800d12f74d8b05e9b89836f-Paper.pdf
- [25] M. Bhardwaj, B. Sundaralingam, A. Mousavian, N. D. Ratliff, D. Fox, F. Ramos, and B. Boots, “Storm: An integrated framework for fast joint-space model-predictive control for reactive manipulation,” in *Conference on Robot Learning*. PMLR, 2022, pp. 750–759.
- [26] J. Bradbury, R. Frostig, P. Hawkins, M. J. Johnson, C. Leary, D. Maclaurin, G. Necula, A. Paszke, J. VanderPlas, S. Wanderman-Milne, and Q. Zhang, “JAX: composable transformations of Python+NumPy programs,” 2018. [Online]. Available: <http://github.com/google/jax>
- [27] D. Fox, W. Burgard, and S. Thrun, “The dynamic window approach to collision avoidance,” *IEEE Robotics & Automation Magazine*, vol. 4, no. 1, pp. 23–33, 1997.